# A Systematic Study and Framework of Fringe Projection Profilometry with Improved Measurement Performance for in-situ LPBF Process Monitoring

Haolin Zhang[+], Chaitanya Krishna Prasad Vallabh[+], Yubo Xiong and Xiayun Zhao*

ZXY Intelligent Precision - Advanced Manufacturing (ZIP-AM) Laboratory

Department of Mechanical Engineering & Materials Science

University of Pittsburgh, Pittsburgh, PA 15261

[+]Both Authors contributed equally

*Authors to whom the correspondence should be addressed

Email: xiayun.zhao@pitt.edu | Phone: (412) 648-4320

Abstract

Fringe Projection Profilometry (FPP) is a cost-effective and non-invasive technology that has been shown to measure finer features. In this work, we developed an in-situ FPP method to measure the dynamic topography of powder bed and printed layer during Laser Powder Bed Fusion (LPBF) additive manufacturing (AM) process. A systematic study towards developing a comprehensive framework of LPBF-specific FPP is demonstrated to enhance and evaluate the performance of applying FPP for in-situ LPBF monitoring, including 1) a modified sensor model with localized correction; 2) improved phase unwrapping with FFT filtering 3) quantitative uncertainty analysis; and 4) experimental validation with ex-situ characterization. The developed LPBF-specific FPP system and methods are implemented on a commercial LPBF-AM machine, achieving better accuracy, more robustness, and increased field of view while maintaining sufficient measurement range and decent resolution, in contrast to literature methods. The established FPP framework will facilitate the development of closed-loop control strategies for advancing LPBF based AM.

Keywords: **Fringe Projection, Sensor Model, Uncertainty Analysis, In-situ Monitoring, Powder Bed Fusion, Additive Manufacturing**

## 1 Introduction

Laser based Additive manufacturing (AM) processes can rapidly and efficiently fabricate three-dimensional (3D) parts of complex shapes and intricate structures, by selectively fusing materials on a layer by layer basis, which are typically hard to achieve using traditional methods. . In recent years, AM processes are being used to produce a myriad of components in various industries including aerospace [1], medical [2], and education [3]. Laser powder bed fusion (LPBF) is one of the most widely used AM techniques for fabricating prototype and near-ready metallic parts. In a LPBF process, a thin layer of powder is evenly spread onto a substrate plate, followed by a selective laser melting, typically using a laser to fuse a cross-section corresponding to the target part geometry [4].Then, the build plate is lowered by a certain height corresponding to a certain layer thickness. A new round of powder spreading, laser scanning, and platform descent is repeated layer after layer until the final product is printed. This whole process takes place inside a chamber, which is tightly sealed and purged with an inert gas such as Argon. Like other AM techniques, LPBF is limited in accuracy and precision [5, 6]. LPBF processes are prone to produce porous defects that can undermine the mechanical properties and performance of printed parts, necessitating the development of in-situ metrology to provide insights into process dynamics and deviations and thus feedback information for developing advanced process control for compensating or even correcting the detected anomalies.

In general, there are two classes of in-situ metrology strategies for LPBF processes, namely, melt pool and powder bed monitoring. Related studies mainly include in-situ melt pool temperature profile [7], and meltpool morphology estimation [8, 9] via an on-axis pyrometer or thermal camera. An off-axis camera system is usually installed outside the build chamber to perform image analysis of the powder bed and the being-printed part for extracting the print part's geometric and surface features [6] along with the powder bed anomalies [10-12]. Specifically for powder bed monitoring, the existing in-situ metrology methods based on camera imaging are limited to obtaining only 2D information of powder layer and printed profile, while quantitative measurement of the vertical thickness is desired but unavailable. Most commercial optical profilers can provide high resolution (submicron) topography for a small area (~0.5× 0.5 mm), such as Keyence Optical profiler, Zygo Optical profiler, and Bruker Contour GT Optical profiler. However, they cannot be integrated onto a LPBF machine due to their size, short working distance, smaller region-of-interests (ROI), and low speed. Fringe Projection Profilometry (FPP) techniques have been used to measure 3D surfaces in diverse areas including human face recognition [13, 14], 3D intra-oral dental profile measurements [15], and surface roughness measurement [16]. In contrast, FPP is well-known for its ability to provide high-resolution and full-field 3D map of the measured objects in a non-contact manner and within a short period of time. Therefore, FPP has a potential to offer a viable approach for in-situ monitoring and measurement of powder bed topography.

Researchers have reported some preliminary work implementing FPP for LPBF process monitoring, but without fully considering the unique LPBF process characteristics (e.g., surface reflectance and build location effect) or with limited measurement performance [17, 18]. Moreover, few literature studies specifically focused on FPP measurement's uncertainty analysis for LPBF [19-21]. As shown in Table 1, the state of art work by Zhang et al. [22] and Liu et al. [23] have implemeted a FPP system in LPBF for metal AM , which, however, could not attain a desired combination of wide field of view, high vertical resolution, and height measurement

range. Furthermore, significant variations exist in surface reflectivity among bare substrate, powder particles, and each printed layer due to the variability in the surface textures [24], which would affect the topography of the printed area and powder area. In this paper, we present a LPBF-specific FPP measurement model and data analytics method considering the localized correction factor which incorporates surface reflectivity, projector and camera's nonlinearity as well as a first-of-its-kind uncertainty quantification for understanding the capability of using FPP to measure in situ both the surface topography of powder bed and the height profile of printed region. We also develop an in-house FPP for in-situ monitoring, on a commercial laser LPBF machine (EOS M290) and implement the developed LPBF-specific FPP (LPBF-FPP) measurement model and algorithms to achieve all the desired measurement performance metrics simultaneously as shown in Table 1.

**Table 1. Comparison to the State of Art Fringe Projection Technology for additive manufacturing**

| Related research | Field of View | Lateral Measurement Resolution | Height Measurement Range |
|---|---|---|---|
| Zhang et al. 2016 [22] | 28 × 15 mm | Micron level | ± 200 μm |
| Liu et al. 2020 [23] | 140 × 140 mm | Millimeter level | More than 10 mm |
| | 3.3 × 8.3 mm | 10 μm | Not reported |
| This work | 110 × 150 mm | Below 40 μm | ± 350 μm |

A general FPP measurement procedure consists of the following steps: (1) project a sequence of structured patterns, typically, sinusoidal fringes or defocused binary fringes onto a target object, (2) capture images of the measured object with projected patterns that are deformed due to the surface height variation of the object, (3) evaluate the height profile in terms of phase values by using inverse trigonometric functions, (4) implement a phase unwrapping algorithm to obtain a continuous phase map of the target object, and (5) calibrate the specific FPP system to convert the unwrapped phase map to a thickness profile. Herein, it is worth pointing out that we take an initiative to modify the conventional FPP model and procedure to account for the special LPBF environment and dynamical process (e.g., layer switchover). Specifically, the projection and camera viewing angles of different print locations vary across the build plate. During a LPBF process, the to-be-measured powder bed will consist of a layer of powder or a mixture of powder and fused part alternately, exhibiting non-uniform surface angle and optical properties such as reflectivity and absorpotion. Also, the LPBF build platform frequently moves down, introducing uncertainty to the measurand plane position. With all these potential error sources, existing literature methods have to be revised and quantitative analysis must be performed to achieve satisfactory measurement accuracy and confidence.

The remainder of the paper is organized as follows. First, we elucidate the measurement theory followed by our modified sensor model and improved data analytics method in Section 2. Then, the measurement uncertainty analysis method are presented in Section 3. In Section 4, the experimental setup, method and the results validating the developed FPP system and methods are reported. Finally, the conclusion and recommendations of this work are presented in Section 5.

## 2 LPBF-specific Fringe Projection Profilometry (FPP) Method

In this section, we will examine the fundamental principle of FPP, elucidate a measurement model, and solve it with experimental calibration as well as analytical methods in the context of LPBF processing to measure the thickness/height profile of a target object (e.g., printed part and powder layer).

### 2.1 Fundamental Principles of Fringe Projection Profilometry

The fundamental step of FPP is to compare a fringe pattern reflected from a target object against that reflected from a reference surface, for extracting the information of the target object. The fringes reflected from the target object are distorted compared to the reference surface, mainly due to the surface properties and the height differences between the two surfaces. The fringe phase value for each pixel is related to the spatial distribution of fringe intensity and is encoded with the target object's dimensional information.

To translate the phase value for each pixel, we apply the theorem of similar triangles to evaluate the geometrical relationship and calculate the height value of each pixel of the camera image. The 2D schematic of the FPP system along with the geometrical relations of the reference and the target object are illustrated in Figure 1. It should be noted that this schematic is not intended to represent a ray-tracing model or a pin-hole model, this illustration is shown to explain the mathematical relations for the similar triangles as explained below.

A light beam is projected from the projector sensor *P* and is incident at point *A* on the reference plane, then the reflected beam will be captured by the camera sensor *C*. Here both the projector and the camera are assumed as the point sources based on the sensor sizes (both have ~1″ sensors) and the working distances. If the target object is placed on top of the reference plane (e.g., a voxel), the light beam is blocked, and the reflected light (red dotted line in Fig. 1) intensity captured by the camera sensor *C* is actually from the pixel on projector $\Delta x$ away from the original pixel (see Figure 1). It has to be noted that the $\Delta x$ << *L*, which is the distance between the two sensors *P* and *C*. Since a sinusoidal fringe pattern is projected in this study, the $\Delta x$ can be related to the phase value change $\Delta\phi$ which is defined in Equation (1). And the relationship can be expressed as:

$$\Delta\phi = \phi_{Obj} - \phi_{Ref} \tag{1}$$

where $\phi_{Obj}$ and $\phi_{Ref}$ are phase values of the fringes reflected from the object and the reference, respectively.

Each pixel's fringe phase values ($\phi_{Obj}$ and $\phi_{Ref}$) can be retrieved through a phase shifting algorithm and a phase unwrapping algorithm that will be discussed in detail in Section 2.3.

$$\frac{\Delta\phi}{2\pi} = \frac{\Delta x}{p}, \rightarrow \Delta x = \frac{p}{2\pi} \times \Delta\phi \tag{2}$$

where $p$ is the pitch length of the projected fringe pattern, which is the distance between two adjacent fringes, also known as the spatial period of the projected fringes, and $\Delta\phi$ is the phase

change expressed in radians. Hence, with a known $\Delta x$, the height value can be calculated using the similar triangles theorem [25, 26] between $\Delta \mathrm{P}OC$ and $\Delta \mathrm{A}OB$ (see Figure 1). The equation is expressed as:

$$\frac{H-z}{z} = \frac{L}{B-A}, \rightarrow z = \frac{(H-z)}{L}\Delta x$$
$$z = \frac{\Delta x H}{L+\Delta x} \rightarrow \frac{\Delta x H/L}{(L+\Delta x)/L} = \frac{\Delta x H}{L};\ (since\ \Delta x << L) \quad \textbf{(3)}$$

As illustrated in Figure 1, $H$ is the distance between the optical devices plane and the reference plane, $z$ is the height value of the target object, $L$ is the distance between projector and camera, and $\Delta x$ is the distance between points A and B.

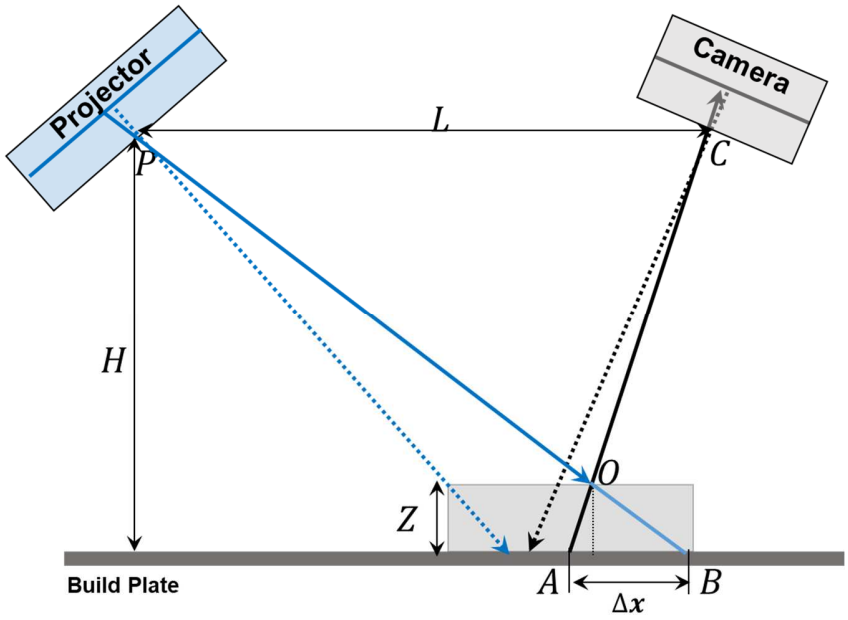


Figure 1. Schematics showing the working of the Fringe Projection Profilometry (FPP) system along with the illustration of a camera pixel capturing a light beam from the reference plane and a light beam from the object voxel. The dashed lines represent the optical axes of the projector and camera. Schematics not-to-scale

By substituting the $\Delta x$ in Equation (3), the height of the target object can be expressed as:

$$Z = \frac{pH}{2\pi L} \times \Delta\phi \quad \textbf{(4)}$$

Note that equation (4) is obtained by considering that all the points $A, B, P, C, O$ in Figure 1 are in the same vertical plane. However, the target object and the reference plane extend laterally, which makes the distance $H$ not a constant but a function $H(x, y)$ that varies with pixel location $x$ and $y$. Hence the height map for the target object can be expressed as:

$$Z(x,y) = K(x,y) \times \Delta\phi(\mathrm{x},\mathrm{y}) \quad \textbf{(5)}$$

where:

$$K(x,y) = \frac{p}{2\pi \cdot L} \times H(x,y) \quad \textbf{(6)}$$

Assuming that the parameters $L$ and $H$ are constant and as the camera sensor size and measured height $Z$ are relatively much smaller, the pitch length $p$ critically determines the sensitivity [27]. Hence, it is necessary to select a sufficiently small pitch length to measure a surface profile at micron level.

### 2.2 Determining the coefficient matrix, $K(x, y)$ via Experimental Calibration

Existing literatures using FPP to LPBF monitoring assume a constant $K$ for the entire target/measurand surface, in our work we employ a spatially resolved $K(x,y)$ to incorporate the potential effects of location-dependent determining factors especially in the scenario of LPBF process as shown in Equation (6). The objective of using $K(x,y)$ instead of a constant $K$ is to establish best practices and methodological framework for improving FPP performance in monitoring the specific LPBF process. The term $K(x,y)$ reflects the sensitivity of the phase change $\Delta\phi$ relative to the height. Intuitively, it can be calculated by plugging in the parameters $L$, $H$, $\theta_P$, and $p$ in Equation (6). A rough measurement of these parameters can provide an approximate prediction of the height value. However, for acquiring an accurate relation between the phase-value and the height-value we perform a system calibration. Herein, we calibrate the phase-to-height conversion for out-of-plane and in-plane separately, which is known as least-square calibration [28].The out-of-plane calibration is the process of converting an unwrapped phase map to a height map for determining the parameter $K(x,y)$ for each pixel in Equation (5). This is done by moving a flat reference plane over a certain height range that covers the height variation of the powder bed. For our system, we use the first powder layer as the reference plane and move the build stage to ten different height positions with increments of 0.1 mm. We define the first height position as 0 mm and move the build stage down to -0.1 mm, -0.2mm, …, -0.9 mm then the unwrapped phase maps are calculated for the ten height positions. For each pixel, the phase values and their corresponding height are fit to a straight line, and the slope, which has unit of millimeter per radian ($mm/rad$), is obtained and assigned to $K(x,y)$ in Equation (5). Figure 2 presents the $K(x,y)$ map across the field of view and the straight-line curve fitting coefficients of the center pixel. The average of the experimentally determined $K(x,y)$ value is 0.114 mm/rad, which is slightly different from the theoretically calculated value of 0.891 mm/rad based on the measured values of the parameters like $L$, $H$, $\theta_P$, and $p$ (see the schematic illustration in Section 4.1) using Equation (6). The primary reason for this variation is the discrepancies in the actual and measured values for these location dependent parameters ($H$ in case of having a build plane that is not perfectly flat, such as the one in this LPBF application case). Thus, given the measurement uncertainty in each pixel location, for data analysis, we use the $K(x,y)$ evaluated from the experimental vertical calibration. As shown in Figure 2, the resulting empirical matrix of $K(x,y)$ displays a spatial variation, please see Fig. S1 for $K(x,y)$ at other locations on the build plate.

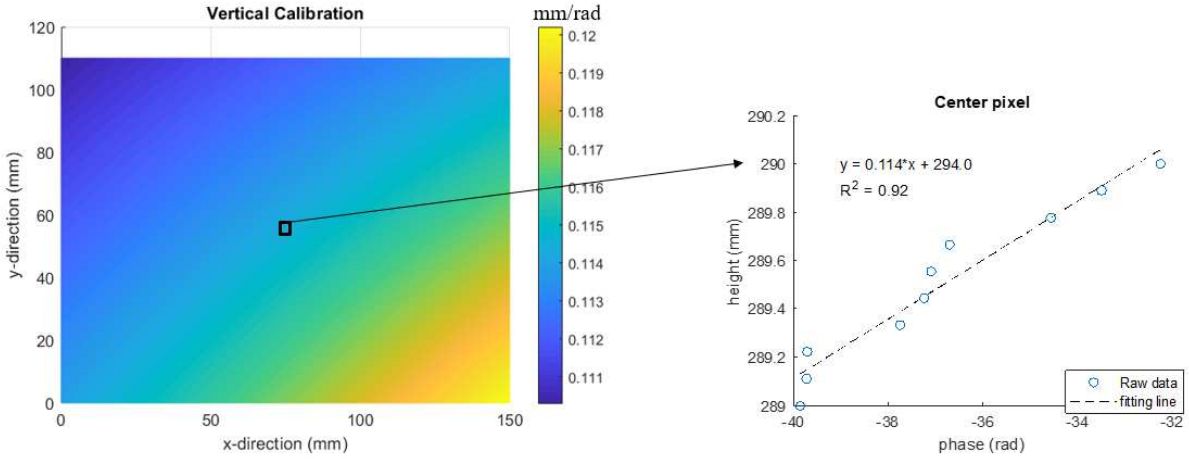


Figure 2. The resulting empirical *K(x,y)* map (left figure) obtained from the experimental calibration, with a close-up illustration (right plot) for determining *K* for the center pixel of the ROI by a linear curve fit to the experimental data

In-plane calibration is the process of converting the lateral map of the captured image from a pixel scale to a X-Y micrometer scale. This is achieved by acquiring the image of a calibration grid plate with accurately measured dimensions. In our case, we placed a flat, printed grid pattern onto the powder bed. A projective transformation matrix $T_{9\times9}$ is created by mapping the coordinates of four corners of the grid plate (see Figure S2 in SI) with the non-orthogonal image taken from the CMOS camera. This perspective correction matrix is determined for each experiment to account for any alignment changes of the experimental setup (camera and the projector) between experiments. The perspective corrected coordinates can be expressed as:

$$[x', y', z'] = T_{9\times9}[x, y, z] \quad \textbf{(7)}$$

Where $[x, y, z]$ is the original image space, while $[x', y', z']$ is the coordinate in orthogonal planar object space [29]. The same transformation matrix is used for performing perspective correction on images obtained from our system for the same projector and camera alignment. The dimension of each square is 5 mm × 5 mm. By counting the number of pixels in a known length, the ratio of pixel scale to X-Y micrometer scale is 38 µm × 38 µm per pixel. This in-plane resolution can be further adjusted by changing the camera's zoom.

## 2.3 Determining phase difference matrix of $\Delta\phi(x, y)$ via Fringe Analysis Algorithms

### 2.3.1 Wrapped phase calculation addressing surface reflectance and location effect in LPBF

From Equation (5), it can be seen that the phase deviation $\Delta\phi(x, y)$ is the input to the FPP model. To obtain $\Delta\phi(x, y)$ in the original projected fringes from the captured images requires some fringe analysis algorithms, including phase shifting and phase unwrapping algorithms. An intuitive way to understand the fringe analysis algorithms is to consider them as a transformation function that converts the images from intensity domain to a phase domain. In the phase shifting algorithm, *N* frames of sinusoidal fringe images are projected onto the target surface, e.g.,

reference plane or object surface. Each frame has an initial phase that is shifted by $2\pi/N$ from the previous frame. The intensity $I_i(x,y)$ for each fringe image pixel $(x, y)$ can be expressed as:

$$I_i(x,y) = B(x,y) + M(x,y) \cdot \cos(\phi(x,y) + \delta_i),\ i = 1,2,\cdots,N \quad \textbf{(8)}$$

Where $i$ is the $i^{th}$ frame, $B(x,y)$ is the background average intensity, $M(x,y)$ is the intensity modulation, $\phi(x,y)$ is the phase value for each pixel, and $\delta$ is the amount of step size shifted between each two adjacent frames that can be described as:

$$\delta_i = 2\pi\frac{i}{N}, \qquad i = 1,2,\dots,N \quad \textbf{(9)}$$

Hence, a total of $N$ equations similar to Equation (8) are used for calculating the phase value $\phi(x,y)$. Conventionally, a least squares algorithm [30] is then implemented to solve for the phase value $\phi(x,y)$ as shown below.

$$\phi(x,y) = arctan\left(\frac{\sum_{i=1}^{N} I_i(x,y) \times sin\left(\frac{2\pi}{N}\times i\right)}{-\sum_{i=1}^{N} I_i(x,y) \times cos\left(\frac{2\pi}{N}\times i\right)}\right) \quad \textbf{(10)}$$

As shown in in Figure **1**, the derived FPP sensor model requires a calculation of spatial shifts in the projected fringe patterns to determine the object height. Therefore, the phase changes $\Delta\phi$ in the original input of a projected fringe (directly related to spatial shifts $\Delta x$) should be determined from the observed light field that is reflected from a target object (e.g., reference or measurand surface). As a matter of fact, especially in the case of LPBF process monitoring, for each camera image pixel $(x,y)$, the pixel's intensity $I^{camera}(x,y)$ is a function of the source intensity from the projector $I^{projector}(x,y)$, the reflecting surface's reflectance $R\ (x,\ y)$, and the camera sensor's response $S(x,y)$ (i.e. ratio of the output and input intensity). Note that $R$ could vary spatially due to the local material and surface properties as well as its location relative to the camera, and $S(x,y)$ could vary with the projected intensity on the measurand surface, and the camera sensor's nonlinearity, therefore $S(x,y)$ can be written as $S_{xy}[S_P, S_C]$ , where $S_P$ and $S_C$ represent the projector and camera non-linearity's respectively. For a reference plane or a measurand surface, the camera image intensity is determined as follows.

$$I^{camera}(x,y) = I^{projector}(x,y) \times R(x,y) \times S_{xy}[S_P, S_C] \quad \textbf{(11)}$$

However, existing methods applying FPP for LPBF monitoring assume $R$ and $S$ to be spatially uniform. To develop a more accurate phase evaluation method for the LPBF-specific FPP, we incorporate a localized correction of the camera image intensity to modify the method of wrapped phase calculation as detailed below. First, we rewrite Equations **Error! Reference source not found.** into the following equations with a correction factor $C_{xy}$ that lumps the effects of both the surface reflectance, projector non-linearity and the camera sensor's nonlinear response. For brevity, we represent this correction factor as $C_{xy}$ in our formulations in this paper.

$$I^{projector}(x,y) = \frac{I^{camera}(x,y)}{R(x,y) \times S_{xy}[S_P, S_C]} = \frac{I^{camera}(x,y)}{C_{xy}} \quad \textbf{(12)}$$

$$C_{xy} \stackrel{\text{def}}{\equiv} R(x,y) \times S_{xy}[S_P, S_C] = \frac{I^{camera}(x,y)}{I^{projector}(x,y)} \quad \textbf{(13)}$$

A 2-way ANOVA was performed to examine the effects of the two factors - projecting intensity and location of the target surface. We confirm that the camera sensed intensity thus the ratio $C_{xy}$ would significantly depend on not only the projected intensity but also the measurand location in the field of view on the LPBF build plate, necessitating the implementation of localized intensity correction in the in-situ FPP monitoring of LPBF. The details of performing ANOVA are presented in Section 2 of the supplementary information.

To obtain the location-dependent $\boldsymbol{C_{xy}}$, since it is difficult to trace the projected source and its intensity for each camera pixel in practice, we estimate a correction function $\widehat{\boldsymbol{C_{xy}}}$ ($\frac{I^{camera}(x,y)}{I^{projector}(x,y)}$) in terms of camera intensity ($I^{camera}(x,y)$) that is directly available. We generate an empirical matrix of the estimated correction function $\widehat{\boldsymbol{C_{xy}}}$ across the field of view by projecting a known intensity-varying sequence of images (each image has all pixels with the same grayscale value between 0 - 255) on to the target plane (where a reference surface or a measurand object will sit) and measuring the camera output intensity reflected from the target plane. To evaluate the ratio for each pixel, we extract the camera captured intensity of each pixel for 20 projected uniform intensity maps ($I_1 = 1, I_2 = 13.7, \ldots, I_{20} = 255$). The ratio of the projected intensity and captured intensity versus the captured intensity is plotted, which is then fit to a curve. This curve fitting information will be used in the model corresponding to the in-situ FPP measurements. A representative plot of this curve fitting is shown in Figure 3. To comprehensively incorporate the effects of projector non-linearity, camera sensor nonlinearity, build location variation, and non-uniform surface reflectance, we generate a matrix of 3000 × 4000 (the same as the resolution of our image data) functions ($I^{Camera}$) for calculating the pixels-wise correction factors $C_{xy}$. A small subset of representative function curves is shown in Figure S4 – S6. It is observed that the value and the relationship with camera intensity for a correction factor $C_{xy}$ significantly vary with the measured pixel location across the build plate (Figs. S4-S6). The goodness of the curve fitting (GOF), i.e., the R-squared value for each pixel is shown as a 3D plot in Figure S7. This unique study further confirms the necessity and importance of improving existing FPP methods by incorporating a detailed pixel-level location-wise correction function to enhance the accuracy of FPP while measuring part and powder topography during a LPBF AM process.

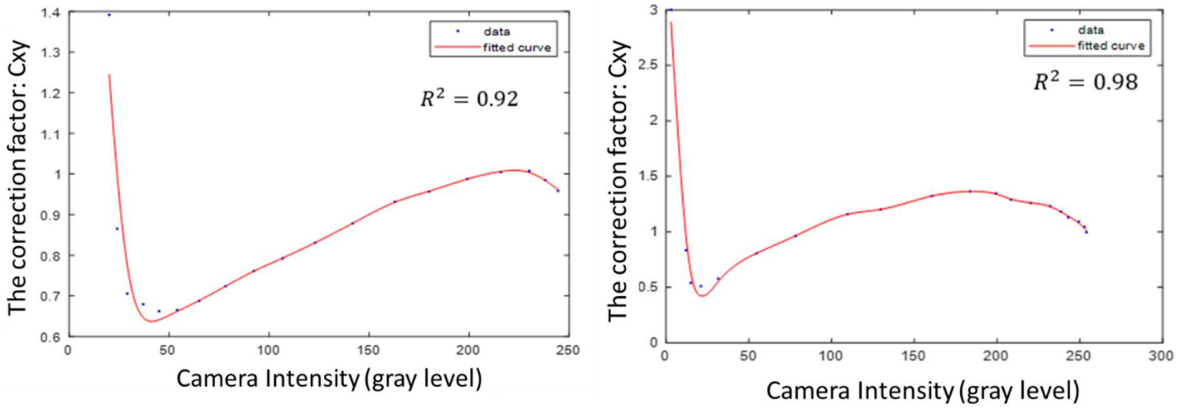


(a) (b)

Figure 3. Plot of the empirical value of $\boldsymbol{C_{xy}}$ vs. camera captured intensity of the center pixel for (a) powder surface and (b) printed surface.

Specifically, in the context of this study (based on Equation (10)) the original phase value of a source light beam that corresponds to a pixel (*x, y*) in the camera image of a reference or a measured object surface, is explicitly calculated as below.

$$\phi_{xy}(I_i^{camera}(x,y)|i=1,\cdots,N) \approx arctan\left(\frac{\sum_{i=1}^{N}\frac{I_i^{camera}(x,y)}{\widehat{C_{xy}}\left(I_i^{camera}(x,y)\right)}\times sin\left(\frac{2\pi}{N}\times i\right)}{-\sum_{i=1}^{N}\frac{I_i^{camera}(x,y)}{\widehat{C_{xy}}\left(I_i^{camera}(x,y)\right)}\times cos\left(\frac{2\pi}{N}\times i\right)}\right) \quad \textbf{(14)}$$

where $I_i^{camera}$ is the light beam intensity captured by the camera for a reference plane or a measurand object surface, with the $i^{th}$ phase shifting fringe pattern. The measurement result of modified wrapped phase calculation method is compared against the traditional phase shifting method by an experiment study as detailed in Section 4.3. Once we obtain the phase map $\phi(x,y)$ for both reference plane and the plane with target object, the phase deviation can be calculated by subtracting the reference phase map ($\phi_{ref}$) from the target plane phase map ($\phi_{Obj}$): $\Delta\phi(x,y) = \phi_{Obj}(x,y) - \phi_{Ref}(x,y)$. However, it is noted that the output of *arctangent* function is restricted in the range of $[-\pi,\pi]$. The phase of sinusoidal function should be continuous. To extend the phase range, phase unwrapping algorithm must be implemented to unfold the phase jump as elaborated in the next section.

### 2.3.2 Phase unwrapping algorithm using a Discrete Fourier filter

Unwrapping phase aims to unfold all the phase jumps in the wrapped phase map. In [31], the authors describe a fast and straightforward method to unfold all the phase jumps that are bigger than $\pi$ along columns and rows correspondingly. However, this method is extremely sensitive to noise in a wrapped phase map. Thus, Kemao et al [32], proposed a windowed Fourier filtered and quality guided phase unwrapping algorithms. In this algorithm, a wrapped phase map is first

converted to its exponential phase field and filtered by a windowed Fourier transform. The filtered amplitude is used as a real valued quality map to guide the phase-unwrapping path. Different window sizes in the window Fourier transform filter are selected to solve different phase unwrapping challenges. The filtered phase map is then used for phase unfolding. Although this phase unwrapping algorithm is robust, it is time-consuming especially for images from a high-resolution camera. Hence, this algorithm is not appropriate for in-situ LPBF monitoring that requires fast metrology. Other researchers introduced a reference-guided phase unwrapping algorithm [22]. This algorithm first calculates the reference phase map that is obtained from the reference plane (powder surface) in LPBF process by unfolding the phase jumps using *unwrap* function from MATLAB's signal processing toolbox. The reference guided phase unwrapping algorithm can be expressed as:

$$\phi_{xy_{Unwrapped}} = \phi_{xy_{Wrapped}} + 2\pi \times Round\left(\frac{\phi_{xy_{Ref}} - \phi_{xy_{Wrapped}}}{2\pi}\right) \quad \textbf{(15)}$$

where $\phi_{xy_{Unwrapped}}$ is the unwrapped phase at pixel $(x,y)$, $\phi_{xy_{Wrapped}}$ is the corresponding wrapped phase, $\phi_{xy_{Ref}}$ is the reference phase, and the $Round$ operator is to round the values in the bracket to the nearest integer. While measuring a powder bed surface in LPBF, all the measurements are taken at around the same height level, and thus the height variation is extremely small (no more than 100 $\mu m$). The reference-guided phase unwrapping is relatively fast compared to windowed Fourier filter phase unwrapping, and less sensitive to noise than simply using two direction unfolding [31]. However, it is still prone to a certain degree of periodical error caused by phase unwrapping.

In this work, we first implement the reference-guided phase unwrapping algorithm to unwrap the reference plane using a bare build plate in LPBF, which is more similar to the target measurand surface of printed part than powder surface as used in existing methods. As shown in Figure S9 with an unwrapped phase plot along the center line from the reference-guided method, some pixels display an abrupt drop compared with their surrounding pixels. The periodical error can be more clearly observed from Figure S10 (a) obtained by removing the inclined trend of the unwrapped phase map of the test plane $\phi_d$. To reduce the periodic phase unwrapping error, we employ a two-dimensional Fast Fourier Transform (2DFFT) as shown in Figure S11. Firstly, we apply a two-dimensional unfolding algorithm to a flat reference plane; secondly, we apply a third order polynomial fitting to the unwrapped phase of the reference plane; thirdly, we plug the reference unwrapped phase map into Equation (15) to calculate the unwrapped phase map for the target plane; lastly, we remove the incline trend of the unwrapped phase map, implement the two-dimensional Fourier filter to the de-trended phase map, and add the incline trend back to create the unwrapped phase map. A quantitative comparison of the modified phase unwrapping process against the RG guided phase unwrapping algorithm is presented in Section 4.

## 2.4 Summary of the newly developed LPBF-specific FPP method

Figure 4 summarizes the procedure of the developed FPP method for LPBF process monitoring. Firstly, a 3-step sinusoidal fringe patterns (i.e., three images with a phase-shift of $2\pi/3$) are projected onto the reference and the target surface, and the respective reflected images are

acquired using the CMOS camera, for each phase value at least 3 images on the reference and the target object are acquired. Then the average of multiple images for each phase projection is used to perform the wrapped phase calculations, for reducing the adverse effect of the projection fluctuation and imaging noise variances. An improved method of calculating wrapped phases is developed to enhance the FPP measurement accuracy in the application scenario of LPBF by incorporating localized pixel-wise correction functions. These correction functions are derived from an elaborative parameter estimation to capture the effects of projector non-linearity, sensor nonlinearity, measurand location induced light propagation path difference, and surface reflectivity non-uniformity across the powder bed, which are ignored in existing methods. The phase value for each pixel is calculated through the modified sensor model in Equation (14). Then, the resulting phase is unwrapped using the reference guided phase unwrapping algorithm enhanced by applying 2D Fourier filtering to remove the erroneous periodic discontinuity at the junction of two adjacent cycles of wrapped phase, thereby evaluating the phase deviation $\Delta\phi(x, y)$ in Equation (5). Besides, a FPP system calibration (which includes the out-of-plane calibration and in plane calibration) is performed to obtain the $K(x, y)$ value, which is used for obtaining the height $z(x, y)$ from the phase deviation map $\Delta\phi(x, y)$. Experimental validation is performed to demonstrate that the newly developed FPP method can take into account the specific LPBF process characteristics and conditions and thus measure the powder and part surface topography with enhanced accuracy during in-situ monitoring of a LPBF process (detailed in Section 4).

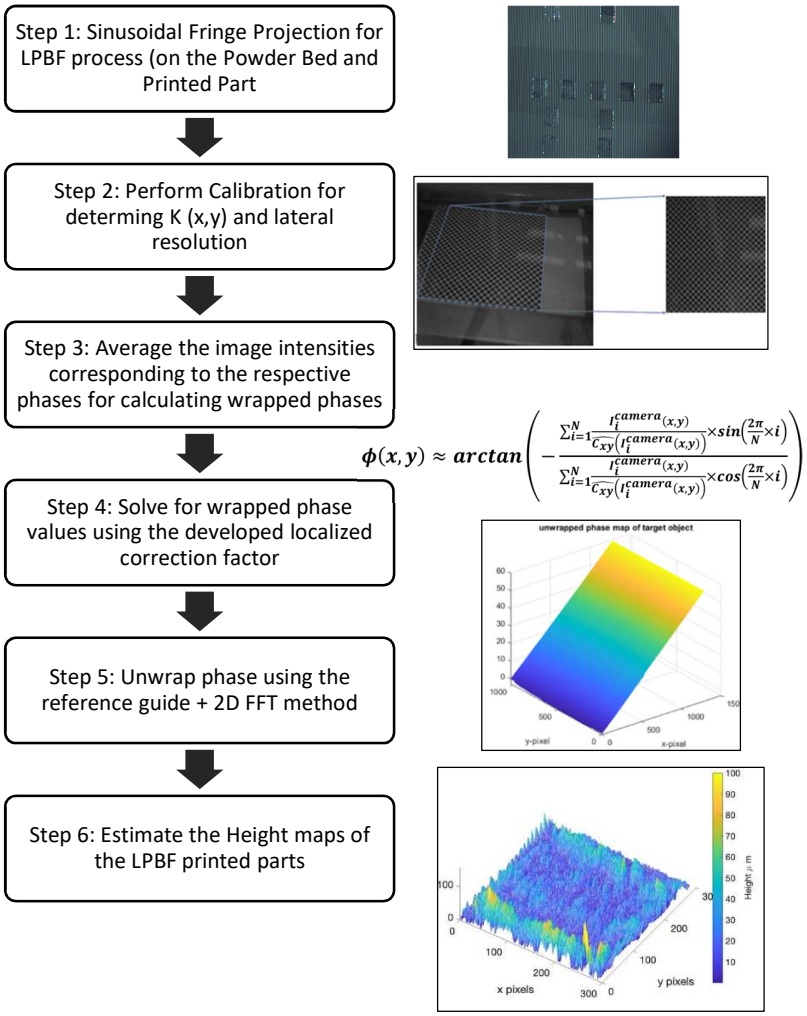


Figure 4: Flow chart of the developed LPBF-specific FPP method

## 3 Measurement Uncertainty Analysis for the Developed FPP Method

From Equation (5), we can conclude that the measurement error mainly comes from two sources. The first source is the process of determining $\boldsymbol{K(x,y)}$ and the second source is the process of determining $\boldsymbol{\Delta\phi(x,y)}$. This section discusses the height measurement uncertainty due to the contribution of these two processes.

### 3.1 Height Measurement Uncertainty due to the error in deriving $\boldsymbol{K(x,y)}$

One source of uncertainty in the height profile measurement is from the out-of-plane calibration process as introduced in Section 2.2. Since the linear regression is used in the estimation of $K(x,y)$, the method of t-distribution is employed to calculate the confidence intervals of $K(x,y)$

with a degree of freedom (DOF) of $n-2=8$ (10 height positions were used to evaluate the slope) [33]. The 95% confidence intervals (*CI*) on the calculated $K(x,y)$ can be expressed as:

$$95\%\ CI\ on\ K(x,y): K\ \pm t_{0.025,8}\ \times S_K \tag{16}$$

where $t_{0.025,8}$ is the t-score at the DOF of 8 and the confident interval *CI* of 95%, and $S_K$ is the standard deviation of the K value that can be determined by:

$$S_k = \sqrt{\frac{s_{y,x}^2}{SS_{xx}}} \tag{17}$$

where $s_{y,x}^2$ is the variance of the $y(x)$ (the height positions in our case, see Figure 2) and expressed as:

$$s_{y,x}^2 = \left(\frac{1}{n-2}\right)\sum_{i=1}^{n}(y_i - \hat{y}_i)^2 \tag{18}$$

where $\hat{y}$ is the linear regression value of the height position (calculated from the fitting line equation), and $SS_{xx}$ is expressed as:

$$SS_{xx} = \sum_{i=1}^{n}(x_i - \bar{x}) \tag{19}$$

where $\bar{x}$ is the mean of independent variables (it is the phase value $\phi$ in our case). Hence, the uncertainty of the K value for each pixel is:

$$U_K(x,y) = t_{0.025,8}\ \times S_K(x,y) \tag{20}$$

Thus, the uncertainty contributed from the calibration process can be mathematically expressed as:

$$U_{Z|K}(x,y) = \frac{\partial Z(x,y)}{\partial K(x,y)} \times U_K(x,y) = \Delta\phi(x,y)\ \times U_k(x,y) \tag{21}$$

### 3.2 Height Measurement Uncertainty due to the error in deriving $\Delta\phi$

For the wrapped phase calculation, the camera captured intensity and the correction factor $\boldsymbol{C_{xy}}$, are the main causes of the height measurement uncertainty. The uncertainty of wrapped phase with respect to the captured intensity and the ratio $\boldsymbol{C_{xy}}$ can be represented as:

$$U_{\phi|\mathrm{I_i}}(x,y) = \frac{\partial \phi}{\partial I_i} \times U_i\,(x,y) \tag{22}$$

$$U_{\phi|\mathrm{C_{xy}}}(x,y) = \frac{\partial \phi}{\partial C_{xy}} \times U_{C_{xy}}(x,y) \tag{23}$$

where the detailed calculations of $\frac{\partial \phi}{\partial I_i}$ and $\frac{\partial \phi}{\partial C_{xy}}$ are shown in Section 5 supplemental information.

Then, the uncertainty of wrapped phase is calculated as below for reference plane and measurand object surface, respectively.

$$U_{\phi_{Ref}} = \sqrt{U_{\phi_{\mathrm{Ref}}|\mathrm{I_i}}(x,y)^2 + U_{\phi_{\mathrm{Ref}}|\mathrm{C_{xy}}}(x,y)^2} \tag{24}$$

$$U_{\phi_{Obj}} = \sqrt{U_{\phi_{Obj}|\mathrm{I_i}}(x,y)^2 + U_{\phi_{\mathrm{Obj}}|\mathrm{C_{xy}}}(x,y)^2} \tag{25}$$

Based on Equation (1), the uncertainty of the total shifted phase $\Delta\boldsymbol{\phi}$ is represented as:

$$U_{\Delta\phi} = \sqrt{U_{\phi_{Ref}}(x,y)^2 + U_{\phi_{Obj}}(x,y)^2} \tag{26}$$

The uncertainty of measured height due to the phase value change is represented as:

$$U_{Z|\Delta\phi} = \frac{\partial Z(x,y)}{\partial \Delta\phi(x,y)} \times U_{\Delta\phi} = K(x,y) \times U_{\Delta\phi} \tag{27}$$

### 3.3 Calculating the overall measurement uncertainty

The uncertainty contributed from the process of determining $\boldsymbol{K(x,y)}$ and the process of phase calculation can be lumped as:

$$U_Z = \sqrt{U_{Z|\phi}^2 + U_{Z|K}^2} \tag{28}$$

Figure S12 shows the uncertainty of each pixel for a pre-printed powder surface (reference plane) and a post-printed surface in height measurement using FPP. It is clearly observed that the uncertainty varies spatially across the whole field of view and the average value of height measurement uncertainty is $\pm\mathbf{12.01}\ \boldsymbol{\mu m}$ for layer-wise powder surface and $\pm\mathbf{19.23}\ \boldsymbol{\mu m}$ for layer-wise printed part surface.

### 3.4 Height measurement Range of the developed system

The uncertainty analysis above does not consider the phase unwrapping algorithm. It is worth noting that the uncertainty due to the phase unwrapping algorithm is negligible only to certain extent. Because the "Round" operator in Equation (15) cannot unwrap a phase correctly when there is a pore or bump that causes the phase deviation from the main trend larger than $\boldsymbol{\pi}$ as illustrated in Figure 5. A phase deviation of $\boldsymbol{\pi}$ corresponds to approximately a height of 358 μm

($\boldsymbol{\pi} \times \mathbf{114}\ \boldsymbol{\mu m/rad}$). Thus, the FPP method can measure heights more accurately within a range of $\pm\,\mathbf{358}\boldsymbol{\mu m}$ as demonstrated in Section 6 of supplementary information. Nevertheless, this effective measurement range is sufficient for monitoring the LPBF powder and printed layer surface profiles which are typically 10's of microns (40µm in the experimental cases presented here).

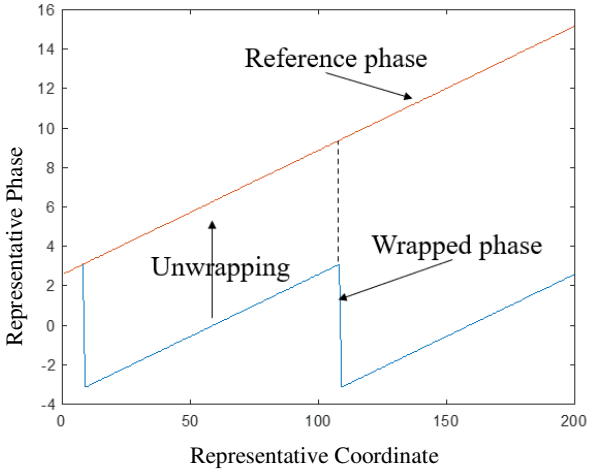


(a)

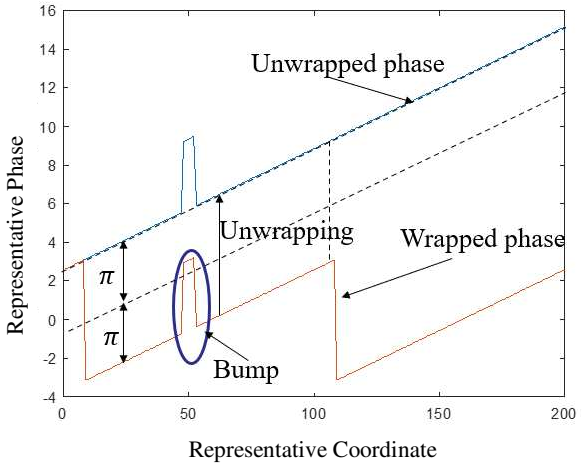


(b)

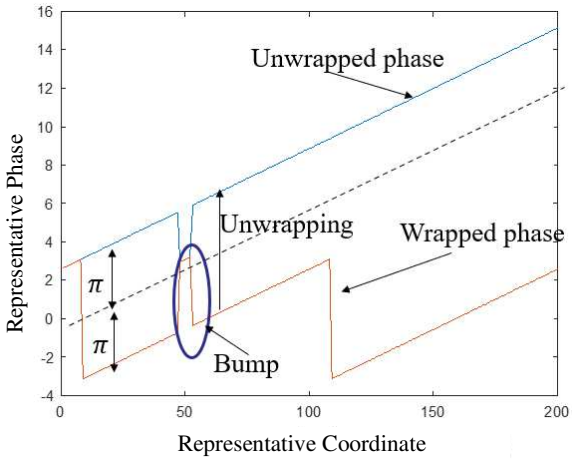


(c)

Figure 5: Demonstration of RG guided phase unwrapping for a flat plane, the phase can be unwrapped correctly using equation (15) as shown in (a). If there is a large bump causing phase deviation from the main trend larger than $\boldsymbol{\pi}$, during the unwrapping, it is supposed to result in the behavior shown in plot (b). However, the distance between reference phase and the wrapped phase is smaller than $\boldsymbol{\pi}$, the "Round" operation will not identify the phase deviation, leading to an underestimated height as shown in (c).

# 4 Experimental Validation

## 4.1 The FPP System Setup and Implementation Procedure for LPBF monitoring

**FPP System Setup**: Our developed FPP system consists of a DLP Projector (LightCrafter 4710 EVM G2, Texas Instruments, Dallas, TX) with a resolution of 1920 ×1080 pixels, a 12 MP CMOS camera (FL3-U3-120S3C-C, Flea3, Teledyne FLIR, Wilsonville, OR) , and a computer to control the two units. The FPP system is mounted on an EOS M290 machine as shown in Figure 6. The printer has a build chamber of 250 × 250 × 325 $mm^3$ and is equipped with a single mode 400W continuous wave ytterbium fiber laser. Detailed design of the FPP system is discussed in the supplemental information.

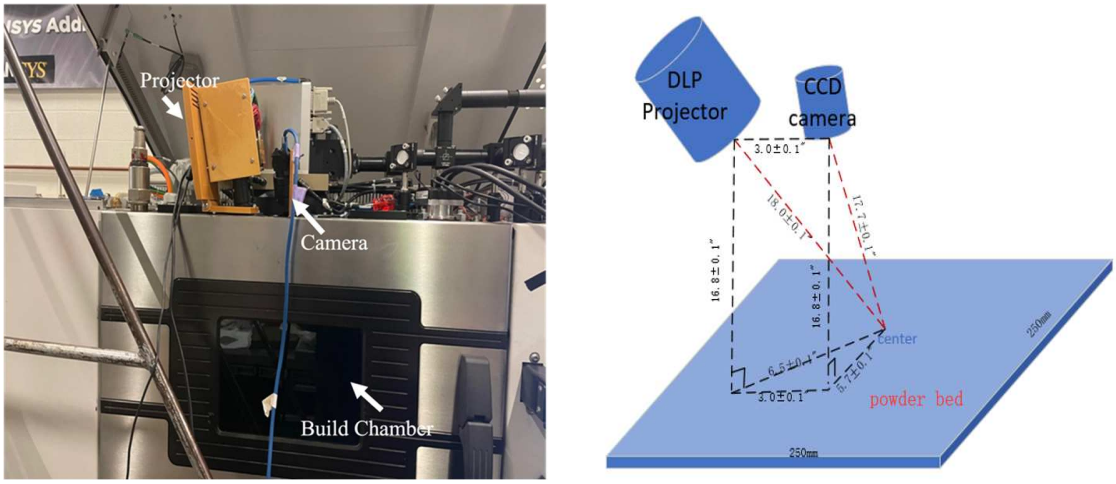


**(a)** **(b)**

Figure 6. Experimental Setup. (a) The physical FPP system built on an EOS M290 DMLS machine. (b) The geometrical schematic of the developed FPP system.

**In-situ FPP Data Acquisition and Analysis**: As shown in Figure S14, to implement the in-situ FPP system for LPBF process monitoring, we take a FPP measurement of the newly coated powder layer as the reference plane for the subsequently printed layer height profile measurement. Then, after the printer prints the corresponding new layer, we take a second FPP measurement of the same field of view that contains the printed area. Lastly, after the build stage is moved down by one-layer thickness (40 µm in this case) to prepare for the next layer powder deposition, we take a third FPP measurement. The powder bed surface images with projected fringes are acquired by the camera at a frame rate of 15 frames-per-second.

For each of the FPP measurements above, three sinusoidal fringe patterns with different phases are projected sequentially and the developed LPBF-specific FPP method (Section 2) is employed to measure the surface topography (Figure S14). And the pixel-resolved layer thickness profile (i.e., a height map of newly printed voxels) is calculated by subtracting the height profile obtained from the third measurement of the previous layer, i.e., Layer # n-1, from the second measurement of the current layer (Layer # n), as illustrated in Figure S15.

## 4.2 Performance Evaluation of the developed FPP Method

To validate the capability of the developed FPP system and methodology for LPBF process monitoring, three sets of experiments are presented with an ex-situ FPP measurement of a staircase sample to evaluate its resolution and accuracy by comparing against standard measurement (this section), and in-situ FPP measurements of square blocks and fatigue specimens to demonstrate its capability of monitoring LPBF process online/in-situ (detailed in the following sections).

In this experiment, a staircase block (15 × 10 × 2 mm) was printed using the EOS M290 DMLS metal AM machine as shown in Figure 7. The sample is designed to have a step increment of 40 µm, same as the default layer thickness to check whether the FPP can vertically resolve the LPBF printed layers. All the samples reported in this work were printed using Inconel 718 alloy powder, commonly referred as IN718 (VDM® Alloy 718, Werdohl, Germany) using default print process parameters (laser power = 285 W, laser scan speed = 960 mm/s) with a powder layer thickness of 40 µm.

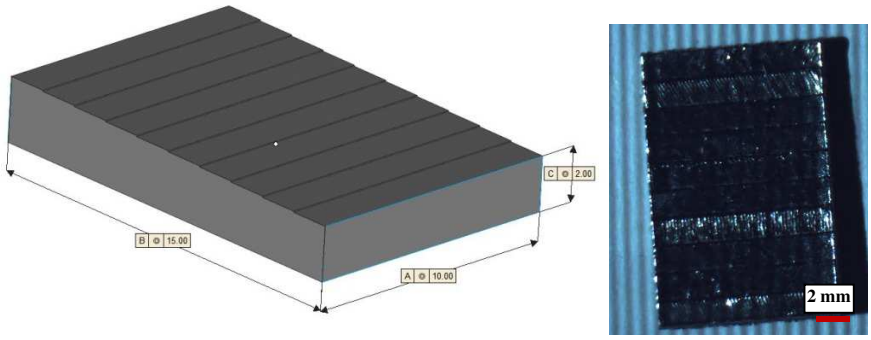


**(a)** **(b)**

Figure 7: (a) the geometrical design of the stair surface (dimensions in mm) and (b) ex-situ fringe projection on the printed sample

To validate the FPP method, the printed sample is measured by the developed FPP and a standard Coordinate Measuring Machine (CMM) (Cyclone Series – 2, Renishaw, West Dundee, IL, USA). However, it is not straightforward to compare the FPP against the CMM due to different data acquisition settings. Our FPP systems acquires around 296,784 data points for the step surface, whereas the CMM machine acquires only 6,488 data points for the same scan region. Therefore, we employ several qualitative and quantitative methods to compare the FPP and the CMM measurements. First, a visual check is conducted by plotting the FPP and CMM measured topographies in the same plot as shown in Figure 8, which shows a good agreement between FPP and CMM. Then, to quantitatively compare the two topographies, we evaluate the measured heights' probability distribution represented as a histogram (a total of 100 intervals with the interval or bin size is 0.007 mm) as shown in Figures S16-17 [34]. The probability for each height value is evaluated by dividing the number of data point at each height value by the total number of data points. A Chi-Square test is conducted with the Chi-Square score calculated as below.

$$\chi^2 = \sum_{i=1}^{100} \frac{(FP_i - CMM_i)}{CMM_i} = 65.56 \quad \textbf{(29)}$$

where $\boldsymbol{FP_i}$ represents the probability density from FPP measured topography at the $i^{th}$ bin (interval), and $\boldsymbol{CMM_i}$ represents the probability density from CMM measured topography at the $i^{th}$ bin (interval). The degree of freedom for Chi-Square test is the number of intervals minus one, i.e., 99 in our case. The critical Chi-Square value at the confidence level of 95% is 77.93, larger than the calculated Chi-Square score of 65.56. Thus, the two probability distributions are statistically the same, validating the accuracy of our developed FPP system.

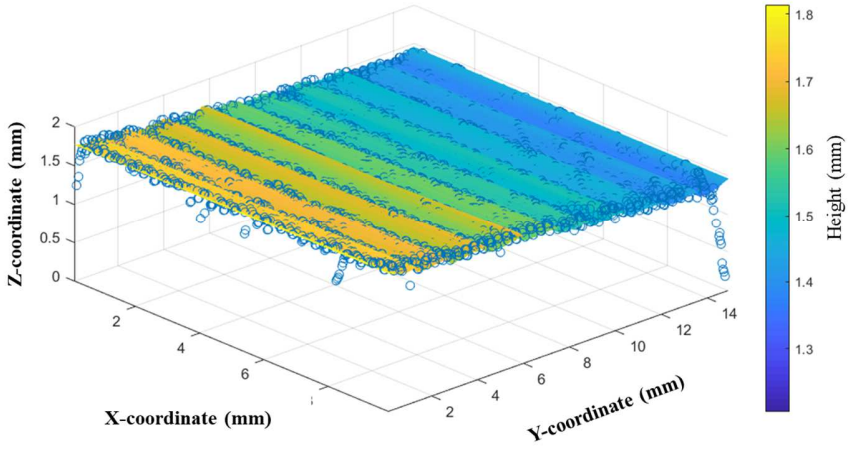


Figure 8: Topography (isometric view) of the staircase sample surface using the CMM (circles) and our FPP (color map) measurements.

### 4.3 Demonstration Case 1: FPP to monitor LPBF printing of Test Blocks

To test the capability of the designed FPP monitoring system in an in-situ printing scenario, a total of 39 blocks with dimensions 10 mm × 10mm and varying heights (40 µm (single layer), 200 µm (five layers) and 800 µm (20 layers)), were printed on a custom 4 × 4-inch IN718 build plate (Fig. 9) using the EOS M290 machine. The reason for this varying print heights is to test the in-situ measurement capability of the developed FPP system in deriving accurate surface topographies along with their height maps. In this work, we just present the data corresponding to a few blocks, the analysis of the other blocks is reserved for a future dissemination.

Figure 9 shows the print schematic along with the raw image acquired during the FPP experiments, prior to perspective transformation. Figure 9(c) shows the printed samples on the build plate. Due to the current setup limitation, the camera is not able to capture all the printing blocks of the experiment. In this section, the focus is to present the importance of the pixel-wise

correction factor (as discussed in Section 2.3.1) and its effect on the accuracy of calculated height maps. The effectiveness of applying 2D FFT filter to eliminate the periodic error during the phase unwrapping stage is also shown via experimental data analysis. First, a block-wise correction factor function is applied in analyzing the experiment data, to save the overall computation cost. To present the importance of the pixel-wise correction factor and to solve for the nonlinearity effects caused by both the projector and camera response, the correction functions between the selected blocks (center block and corner block) are compared and applied for deriving the height maps. Figure 10 shows the selected blocks, the block with orange contour is referred as center block and the blocks with blue and green contours are referred as corner blocks in the analysis below.

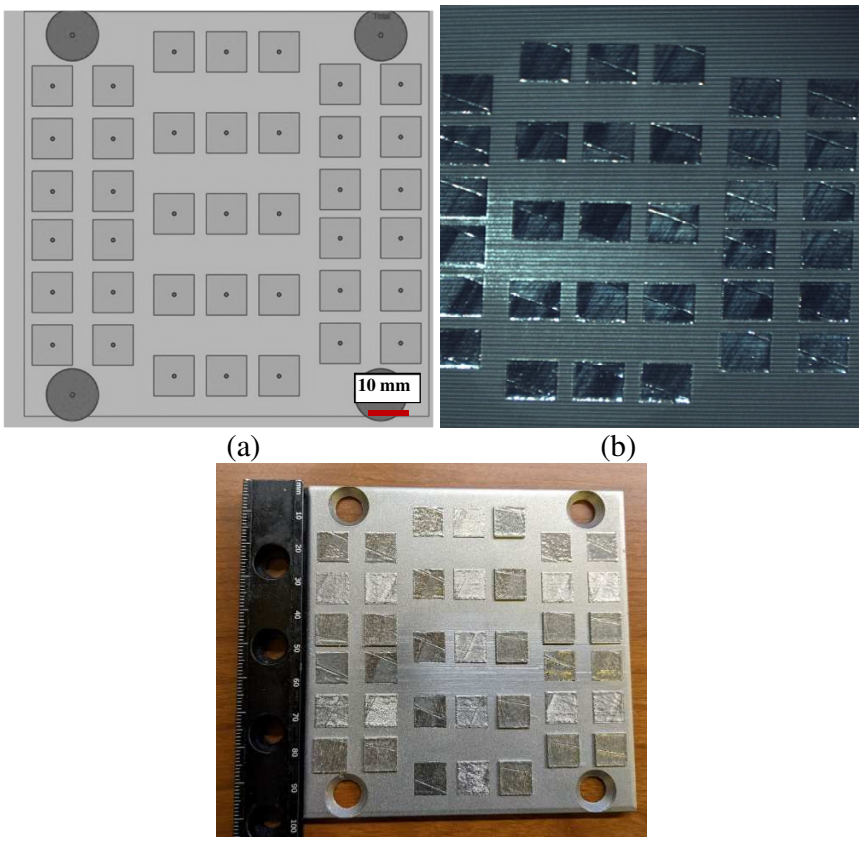


Figure 9: a) Schematic of the block printing experiment, each block has lateral dimensions of 10 × 10 mm, b) raw image of the print acquired during the experiment, prior to perspective correction, and (c) image of the printed samples

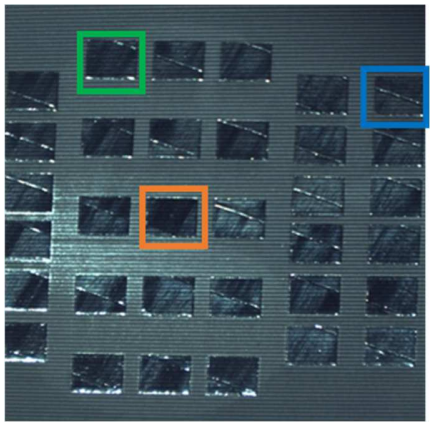

Figure 10: Image showing the chosen Center and Corner blocks in the camera's FOV for demonstrating the importance of pixel-wise correction factor in deriving the height maps.

The corresponding correction factor (curve fitting) for each selected block is shown in Fig. 11 (a - b). It can be observed that the correction factor function curve significantly depends on the pixel location and the fitting curve at the center location is not applicable for the corner locations. The height maps of the center block using two different correction fitting curves are shown in Figure 11 (c) and (d). Figure 11 (c) is specifically the height map of the right corner block using its corresponding correction factor (blue block in Fig. 10), And Figure 11 (d) is the height map of the same corner block derived using the center correction factor (center block – orange boundary in Fig. 10), here it can be noted that the height map has observable periodic error and height aberrations when compared to Fig. 11(c). Thus, validating the need of localized correction factor for LPBF-specific FPP measurements. The implementation of localized fitting curve effectively eliminates the nonlinear/periodic error introduced by reflectance, projector non-linearity and camera response.

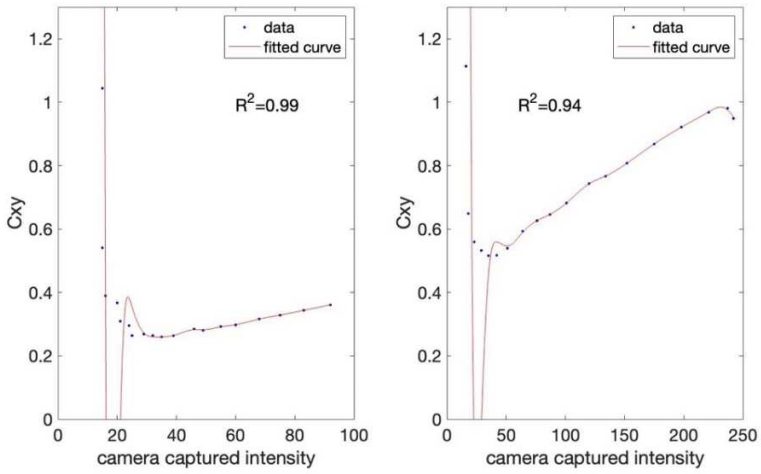


(a) (b)

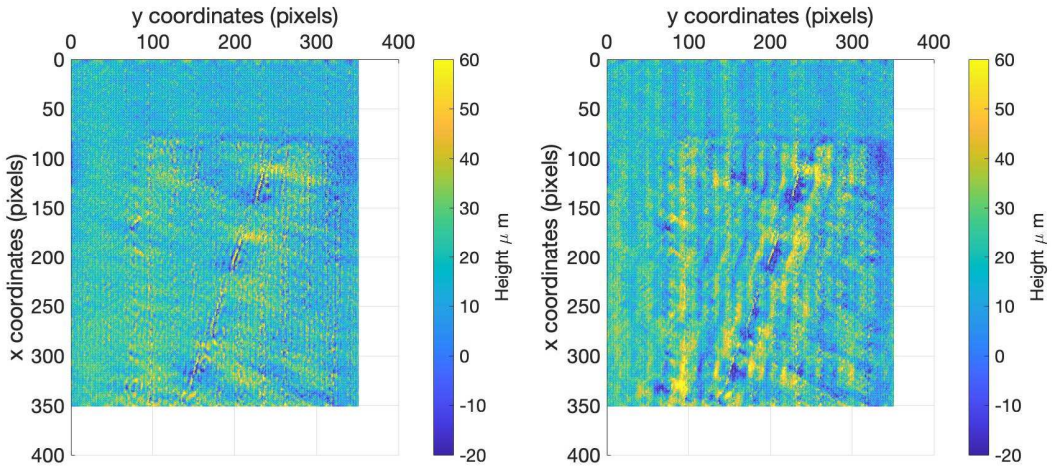


(c) (d)

Figure 11: (a) The correction factor curve for right corner block. (b) The correction factor curve for center block. (c) Height map of right corner block using the right corner correction factor fitting curve. (d) Height map of center block using the right corner correction factor fitting curve

Another major novelty of the designed FPP monitoring system is the application of 2DFFT filter to eliminate the unwrapping phase error/periodic error. The proposed 2DFFT phase unwrapping technique is compared with the reference guided algorithm by analyzing the experimental block data. Although the reference guided algorithm provides relatively fast approach to unfold the phase jump in the phase map, it is easily affected by the noise from the acquired images especially in an in-situ printing scenario where the build chamber has varying circumstances (non-uniform spread of powder and intensity saturation from metal surfaces). Figure 12 (a) shows that the sectioned unwrapped phase plot consists of periodic phase error/fluctuations caused by the reference guided algorithm described in Section 2, which further emphasizes the sensitivity of FPP monitoring system in the in-situ printing environment and necessity to address such issues. By applying the reference guided phase unwrapping strategy combined with 2DFFT, the unwrapped phase becomes smooth and most of the errors and noises are eliminated effectively, as shown in Figure 12 (b).

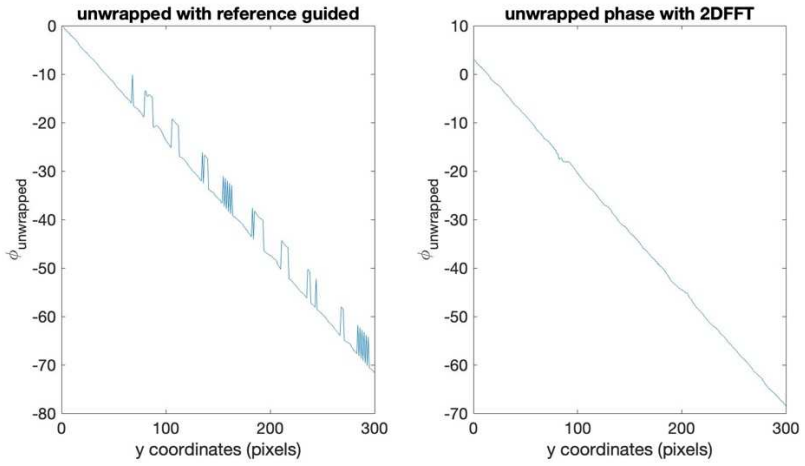


(a) (b)

Figure 12: (a) Unwrapped phase plot using only reference guided algorithm (b) unwrapped phase using the proposed 2DFFT algorithm combined with reference guided

By combining the localized correction factor fitting and 2D FFT filter, we could effectively reduce the periodic error in the resulting height maps. In the analysis below, the height maps of right block enclosed in green boundary in Figure 10 are obtained using both the proposed pixel-wise correction factor plus 2DFFT algorithm (Fig. 13 (a)) and the traditional approach using center pixel correction factor with reference-guided phase unwrapping algorithm (Fig. 13 (b)). The two obtained height maps are compared with the ex-situ measurements (Fig. 13 (c)) from Keyence 3D profilometer/microscope (Keyence VR3200, Keyence Corporation of America, IL, USA) to validate the surface topography characteristics obtained from FPP system. Since the Keyence instrument we use only allows extracting the line profile of the surface topography along with their surface maps, we validated the line profiles of the sample height and the surface topography, qualitatively.

Figure 13 (a-c) show the qualitative surface topography and height maps comparison of the FPP derived profiles and the Keyence profilometer profile. Here we compare a printed block with a specified height of 40 µm (i.e., a single layer print – block demarcated with green boundary in Fig. 10). Qualitatively, both the height maps in Fig. 13 (a) and 13 (b) exhibit similar topographical characteristics. However, Fig. 13 (c) shows a large variation in the surface topography and height maps compared to Fig. 13 (b). As detailed above, Fig. 13 (a) and (c) correspond to the surface topography of the same print block but processed using different $C_{xy}$ factors and with/without 2D FFT.

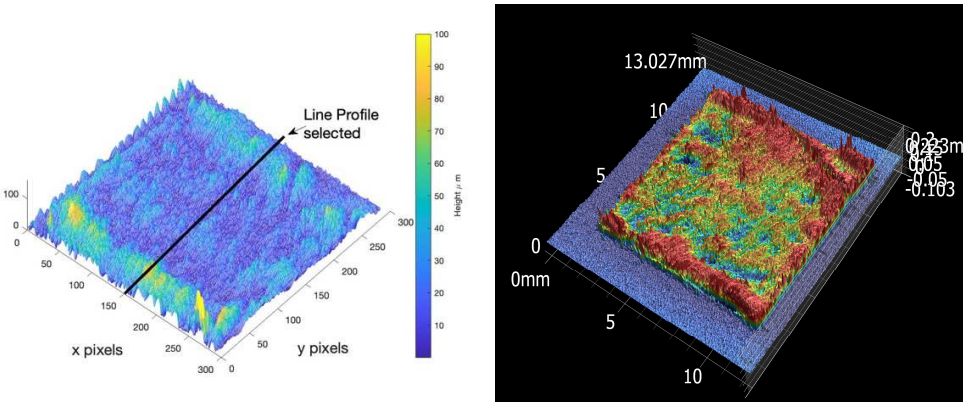


(a) (b)

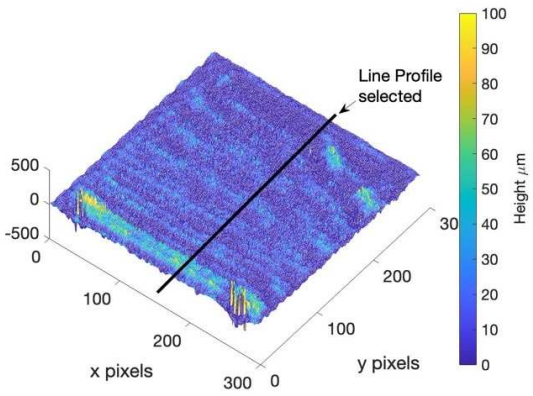


(c)

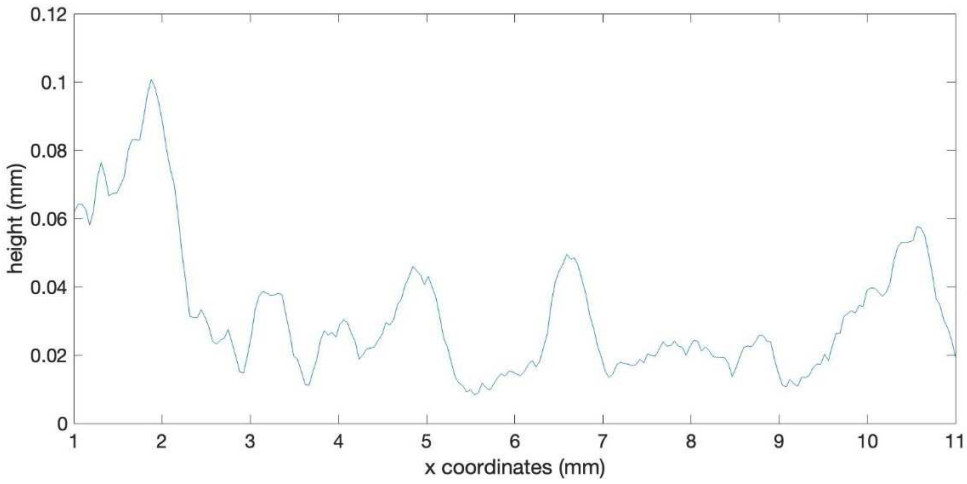


(d)

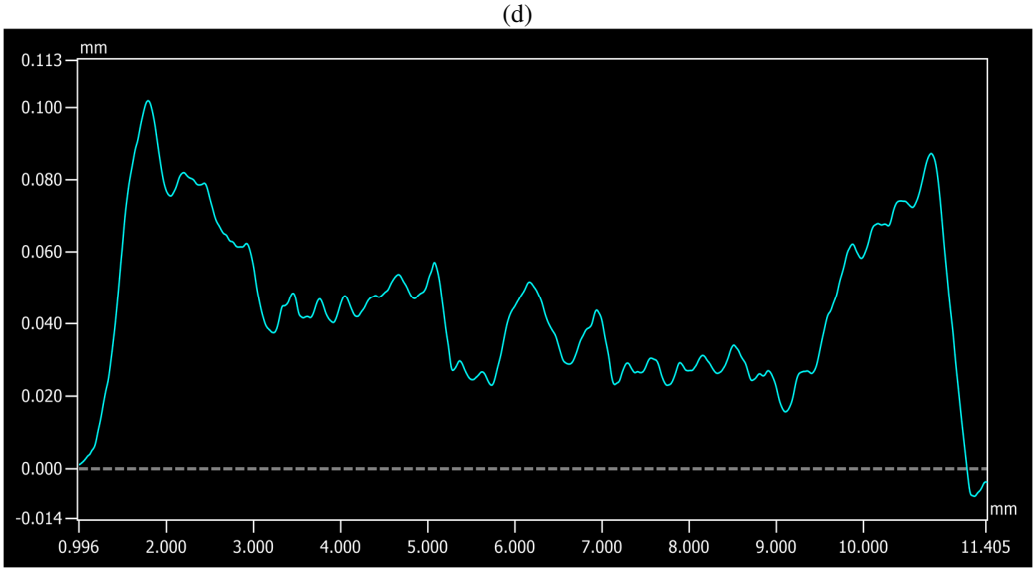


(e)

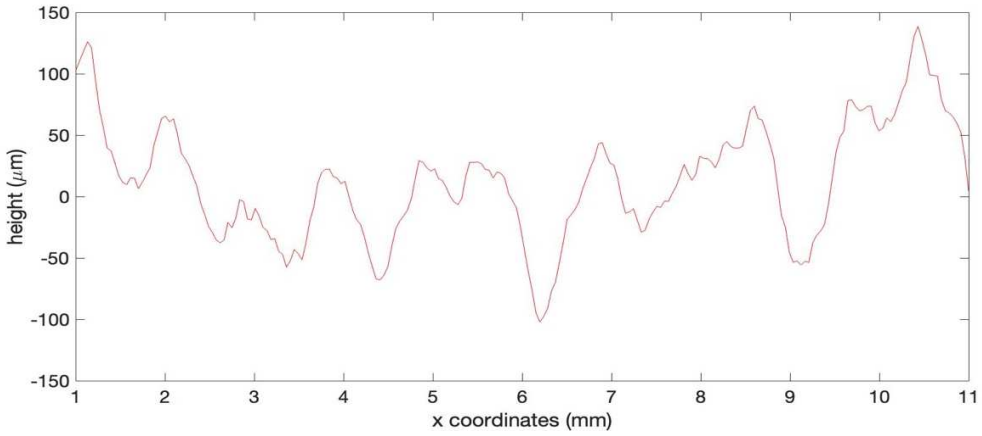


(f)

Figure 13: (a) Single layer printed block (green boundary from Figure 10) height map from FPP with the corresponding pixel-wise correction factor $C_{xy}$ and 2D FFT(b) same single layer printed block heightmap from

Keyence (c) Single layer printed block (green from Figure 10) height map from FPP using center $C_{xy}$ and 2DFFT (d) FPP line profile for the selected line using pixel-wise Cxy and 2DFFT (e) Keyence line profile for the selected line (f) FPP line profile for the selected line using center $C_{xy}$ without 2D FFT

To further characterize these profiles, Figures 13 (d) and (e) compare the line profiles of the surface topography of the same printed block (green boundary block in Fig. 10). The line profiles (both FPP and Keyence) for comparison are extracted from the near center location on the block – specifically, 5.21 mm from the left edge of the printed block as denoted in Figure 13 (a). By comparing the extracted line height profile between FPP and Keyence microscope, it can be seen that the proposed FPP monitoring algorithm (correction factor ($C_{xy}$) + 2DFFT) and Keyence result present similar essential information of the layer topography. For instance, both FPP and Keyence results reveal the peak height range between 1 to 3 mm, the height valleys between ~5 mm and 6 mm, and the final height increase between 10 mm and 11 mm. The FPP measured profile shows the peak height is 100.7 microns which is similar to the Keyence measured 109 microns. It should be noted that we compare the in-situ measured data with the ex-situ measured data, and there are various factors which can influence the in-situ FPP measured data such as non-uniform spread of powders and the gas flow during the manufacturing process. Despite the influence during the manufacturing process, the designed FPP monitoring system is capable of revealing the dominating surface topography characteristics such as small bump and depth layer-wisely. Further, comparing the line profile using traditional approach (center correction factor without 2DFFT) - Fig. 13 (f), although the beginning and ending parts of the line profile show the increasing trend of heights, the profile is prone to periodic errors and huge fluctuation of heights. The resulting line profile from traditional approach is not capable of accurately capturing the major valley and depth locations as the proposed processing methods. The 20$^{th}$ layer's surface topography of another printed block using designed algorithm is also compared with Keyence profile result to further validate the accuracy of developed FPP monitoring system. As shown in Figure S18, the FPP measured surface topography reveals the major valley locations in the 20$^{th}$ layer exists between 1 mm and 3 mm for this particular printed block.

Further, we also validated the average height obtained from two approaches against the average step height derived from Keyence microscope. The average height profile obtained from Keyence microscope for the tested block in Figure 13, is 42 microns (based on the selected area in Figure 14). The average height obtained from FPP calculated heightmap using proposed pixel-wise correction factor with 2DFFT algorithm is ~40.32 microns which results in 4% difference when compared to the Keyence measurement. The average height obtained from FPP calculated heightmap using center-pixel correction factor without 2DFFT is ~48.6 microns which results in 15.7% difference. The huge deviation from Keyence is primarily caused by the periodic error during the phase unwrapping stage and the nonlinearity that cannot be addressed by simply using center pixel correction factor. In this section, the extracted surface topographies, line profiles and the calculated average height value show the advantage and necessity to apply the pixel-wise correction factor and 2DFFT filter to eliminate the non-linearities and periodic errors.

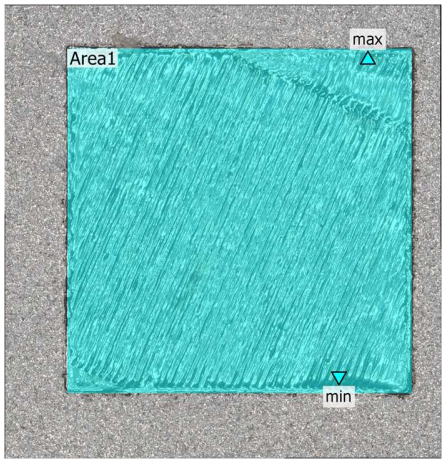

Figure 14: The area profile selected from Keyence for average height evaluation

## 4.4 Demonstration Case 2: FPP to monitor LPBF printing of Fatigue Specimens

Similarly, to demonstrate the applicability of the developed FPP system and methods on a practical test case, we conducted the FPP experiments on a fatigue test specimens print. A total of 5 fatigue test samples were printed using the EOS M290 machine. In this experiment, in-situ FPP monitoring data for a total of 95 layers out of the 100 printed layers were acquired. The data corresponding to five layers were missed during acquisition due to technical issues with the projector and camera. The build design of the fatigue bars and FPP monitored region on the powder bed is shown in Figure 15(a). The in-situ image of the five fatigue bars along with the projected fringe pattern is shown in Figure 15(b). The Figure 15(c) shows the height profile and topography obtained from the developed FPP methods and it can be clearly observed that the average height of the fused area is lower than the powder surface due to solidification and shrinkage of the fused region. In the FPP measured height profile maps, the height variation of the hatching pattern corresponding to each layer can also be observed, this information is not available from the traditional camera imaging approaches.

The FPP measured average measured layer thickness for the monitored 95 layers is $\mathbf{40.48}\ \boldsymbol{\mu m}$, which is close to the preset layer thickness of $\mathbf{40}\ \boldsymbol{\mu m}$. Another simple validation of the in-situ measurement can be done by comparing the overall printed part thickness estimated from the FPP measurement and the measurement with a digital caliper. Since we did not monitor all the layers, the FPP measured thickness values of the monitored 95 layers are added up and linearly extraploated to all the printed layers (100 layers) for evaluating the final printed part thickness as shown in Figure 15(d). The average height of the fatigue bars obtained through this method is 3.97 mm, close to the digital caliper measurement of 3.80 mm, showing that the developed FPP system and methods are capable of in-situ height profile measurement for an actual print scenario in LPBF processes.

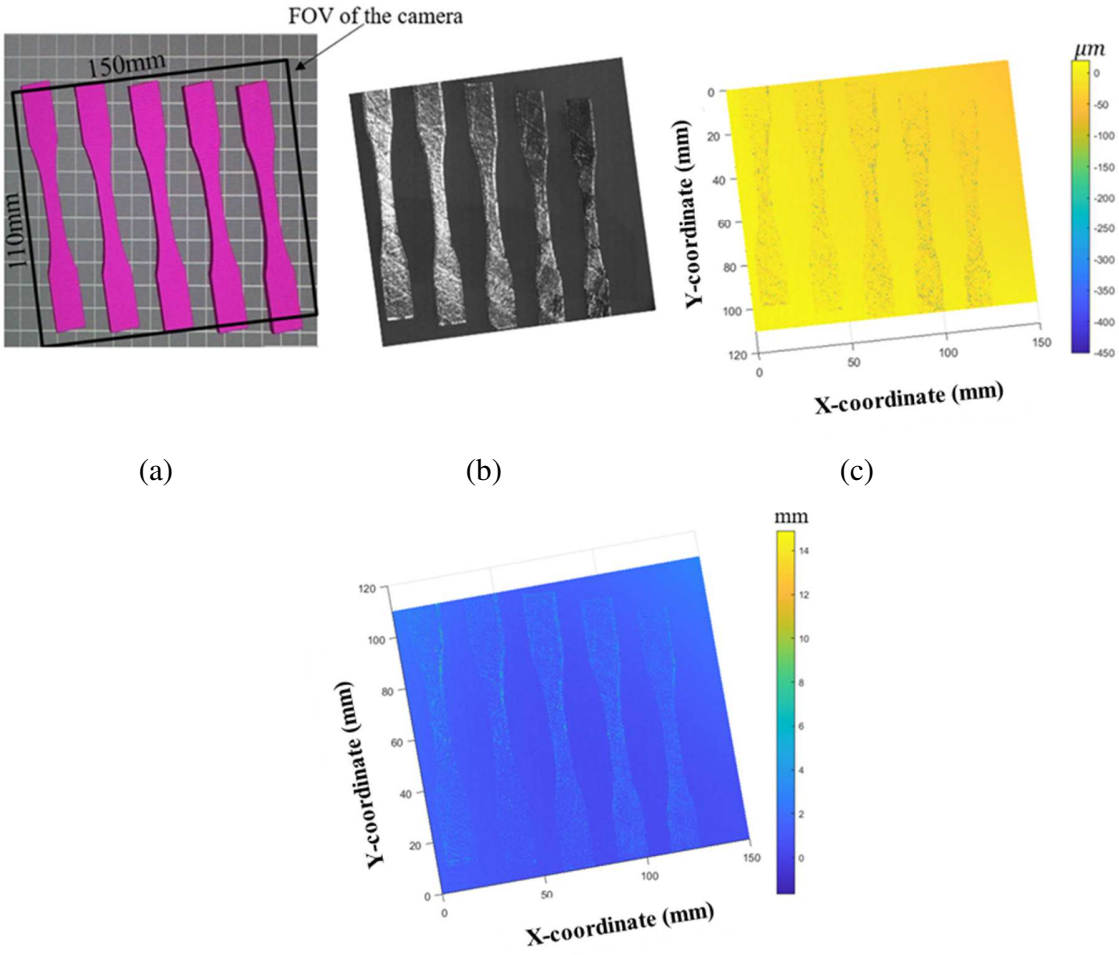


Figure 15: (a) Print schematic of the fatigue bars print, with the demarcation of the camera's field of view (FOV), (b) acquired in-situ FPP image data of the printed surface; (c) in-situ topography of the printed surface; (d) the total height profile of printed samples.

Regarding the computation time of the algorithms and codes, the wrapped phase calculation using the pre-calculated $C_{xy}$, phase unwrapping (reference guided + 2D FFT) and the evaluation of the height maps for each layer takes about 2 minutes (dependent on the field of view). However, the calculation of the localized correction factor $C_{xy}$ (Section 2.3.1) is computationally expensive (~2-4 hours for 3000×4000 pixels) which needs to be calculated only once for a fixed setup (i.e., projector and camera location). Therefore, the computation time for $C_{xy}$ should not be accounted for the layer-wise analysis, resulting in a reasonable computation of less than 2 minutes for each layer on a standard laptop computer. With GPU enabled computing, we anticipate a significant reduction in the computation time for deploying the developed FPP method in situ for real-time data acquisition, processing, and measurement.

## 5 Conclusions and Recommendations

In this work, we established a new framework of FPP sensor modeling and data analytics specifically for the application in LPBF based AM. To the best of our knowledge, this is the first time that a general FPP model is elucidated, enhanced, and evaluated in the unique context of a LPBF processes by incorporating the effects of measurand surface and build location, as well as developing a quantitative measurement uncertainty analysis method. The major novelty of the designed FPP system and methods is the implementation of localized pixel-wise correction factor ($C_{xy}$) to eliminate the nonlinear response of both the projector and the camera, along with the location-dependent reflectance. Besides, to reduce the periodical error in the height measurement, we apply a 2D Fourier filter in the phase unwrapping process that has been shown to improve the resolution of the topography measurement, and remove the periodical errors caused by the reference guided phase unwrapping process. We also developed a custom FPP system on top of a commercial LPBF machine and implemented the developed methodological framework of FPP by measuring a printed part offline as well as monitoring a LPBF process online. The results demonstrated that the newly developed FPP method can measure a field of 110 × 150 mm with a vertical resolution of at least 40 $\mu m$ and lateral resolution of 38 $\mu m$. The average layer-wise uncertainty across of the powder surface and the printed surface in the field of view are 12.01 $\mu m$ and 19.23 $\mu m$, respectively.

A thorough uncertainty analysis is conducted, offering quantitative insights about the FPP error sources and possible improvement directions. Besides, a systematic approach for evaluating the FPP measurement accuracy against standard equipment (e.g., CMM and microscopy) is developed by employing probability distribution test. Along with the improved FPP method (Section 2), these FPP measurement performance evaluation methods (Sections 3 and 4.2) form a comprehensive framework of FPP that can measure the LPBF process with accuracy, robustness, and confidence.

Initial experiment study cases are presented to demonstrate the capability and potential of the developed LPBF-specific framework. Note in these proof-of-concept experiments we only use the $C_{xy}$ calibrated from a powder bed to calculate the surface topographies of both powder bed and printed part. A computationally efficient approach of block-wise $C_{xy}$ is demonstrated, providing an implication of the potential advantage of a pixel-wise $C_{xy}$. In the future, we will fully implement the methods developed in this work by applying powder surface's $C_{xy}$ for powder bed topography and printed sample's $C_{xy}$ for printed part topography, all $C_{xy}$ being refined towards pixel-wise.

The future work of this work will focus on improving the measurement performance of LPBF-specific FPP via machine learning. Specifically, the FPP measured height map of each LPBF printed layer will be processed using an unsupervised convolutional neural network to detect both macroscopic and microscopic defects at each printed layer. A deep convolutional neural network will be implemented to increase the computation speed and accuracy of phase unwrapping [35]. A two-step convolutional neural network structure will be implemented. The first step will apply a to-be-developed deep convolutional neural network to accelerate the FPP phase unwrapping, and the second step will process height maps using unsupervised feature-extraction neural network for defect detection.

Another limitation of the developed FPP system is that the projected light incident on the printed surface will cause saturated and low modulation issues in the captured images. Thus, some of the height information is lost in the saturated areas, causing large uncertainty in height measurement. To increase height measurement resolution and decrease the uncertainty, we plan to implement a modified hardware setup (dual projector setup), multi intensity fringe projection (bright and dark) along with improved imaging processing algorithms (such as intensity adjusting using High Dynamic Range methods). A multi-sensor, multi-view FPP method with two projectors can be employed to mitigate the saturation issue and process the data more accurately [36]. The saturated area will be recorded and compensated by the second angle projection as the saturated areas are expected to shift when projecting from another angle.

Overall, the ultimate LPBF-specific FPP method will enable real-time topography measurement of actual printed layer topography and part geometry, as well as online inspection of process anomaly and part defects. It will offer an affordable, accurate, reliable, and fast online measurement method to facilitate the realization of much-desired real-time control and rapid qualification of LPBF-AM processes.

## 6 Acknowledgements

We would like to thank Mr. Brandon Blasko who greatly helped us with experiments and data acquisition. We are grateful to Prof. Albert To for all his suggestions during the course of this project. We also would like to acknowledge partial support from the Department of Energy University Turbine Systems Research grant (DE-FOA-0001993 Award Number: FE0031774) and the facilities support from ANSYS Additive Manufacturing Research Laboratory (AMRL) at University of Pittsburgh.

## REFERENCES


[1] E. Atzeni, A. Salmi, Economics of additive manufacturing for end-usable metal parts, The International Journal of Advanced Manufacturing Technology 62(9-12) (2012) 1147-1155.
[2] M. Javaid, A. Haleem, Additive manufacturing applications in medical cases: A literature based review, Alexandria Journal of Medicine 54(4) (2018) 411-422.
[3] H.A. Colorado, D.E. Mendoza, F.L. Valencia, A Combined Strategy of Additive Manufacturing to Support Multidisciplinary Education in Arts, Biology, and Engineering, Journal of Science Education and Technology 30(1) (2021) 58-73.
[4] W.E. King, A.T. Anderson, R.M. Ferencz, N.E. Hodge, C. Kamath, S.A. Khairallah, A.M. Rubenchik, Laser powder bed fusion additive manufacturing of metals; physics, computational, and materials challenges, Applied Physics Reviews 2(4) (2015) 041304.
[5] M.A. Anam, D. Pal, B. Stucker, Modeling and experimental validation of nickel-based super alloy (Inconel 625) made using selective laser melting, Solid Freeform Fabrication (SFF) Symposium, University of Texas at Austin, Austin, TX, Aug, 2013, pp. 12-14.
[6] J. zur Jacobsmühlen, S. Kleszczynski, D. Schneider, G. Witt, High resolution imaging for inspection of laser beam melting systems, 2013 IEEE international instrumentation and measurement technology conference (I2MTC), IEEE, 2013, pp. 707-712.
[7] P.A. Hooper, Melt pool temperature and cooling rates in laser powder bed fusion, Additive Manufacturing 22 (2018) 548-559.
[8] S. Clijsters, T. Craeghs, S. Buls, K. Kempen, J.-P. Kruth, In situ quality control of the selective laser melting process using a high-speed, real-time melt pool monitoring system, The International Journal of Advanced Manufacturing Technology 75(5-8) (2014) 1089-1101.
[9] C.K.P. Vallabh, X. Zhao, Continuous Comprehensive Monitoring of Melt Pool Morphology Under Realistic Printing Scenarios with Laser Powder Bed Fusion, 3D Printing and Additive Manufacturing (2021).
[10] L. Scime, J. Beuth, A multi-scale convolutional neural network for autonomous anomaly detection and classification in a laser powder bed fusion additive manufacturing process, Additive Manufacturing 24 (2018) 273-286.
[11] C. Gobert, E.W. Reutzel, J. Petrich, A.R. Nassar, S. Phoha, Application of supervised machine learning for defect detection during metallic powder bed fusion additive manufacturing using high resolution imaging, Additive Manufacturing 21 (2018) 517-528.
[12] C.K.P. Vallabh, Y. Xiong, X. Zhao, In-Situ Monitoring of Laser Powder Bed Fusion Process Anomalies via a Comprehensive Analysis of Off-Axis Camera Data, International Manufacturing Science and Engineering Conference, American Society of Mechanical Engineers, 2020, p. V001T01A041.
[13] G. Zhou, Z. Li, C. Wang, Y. Shi, A novel method for human expression rapid reconstruction, Tsinghua Science & Technology 14 (2009) 62-65.
[14] J. Yagnik, G.S. Siva, K. Ramakrishnan, L.K. Rao, 3D shape extraction of human face in presence of facial hair: A profilometric approach, TENCON 2005-2005 IEEE Region 10 Conference, IEEE, 2005, pp. 1-5.
[15] L.-C. Chen, C.-C. Huang, Miniaturized 3D surface profilometer using digital fringe projection, Measurement Science and Technology 16(5) (2005) 1061.
[16] L.C. Chen, Y.W. Chang, High accuracy confocal full-field 3-D surface profilometry for micro lenses using a digital fringe projection strategy, Key Engineering Materials, Trans Tech Publ, 2008, pp. 113-116.

[17] N. Southon, P. Stavroulakis, R. Goodridge, R. Leach, In-process measurement and monitoring of a polymer laser sintering powder bed with fringe projection, Materials & Design 157 (2018) 227-234.
[18] A. Dickins, T. Widjanarko, D. Sims-Waterhouse, A. Thompson, S. Lawes, N. Senin, R. Leach, Multi-view fringe projection system for surface topography measurement during metal powder bed fusion, JOSA A 37(9) (2020) B93-B105.
[19] P. Stavroulakis, S. Chen, C. Delorme, P. Bointon, G. Tzimiropoulos, R. Leach, Rapid tracking of extrinsic projector parameters in fringe projection using machine learning, Optics and Lasers in Engineering 114 (2019) 7-14.
[20] B. Zhang, A. Davies, C. Evans, J. Ziegert, Validity of the instrument transfer function for fringe projection metrology, Applied optics 57(11) (2018) 2795-2803.
[21] G. Gayton, R. Su, R. Leach, L. Bradley, Uncertainty evaluation of fringe projection based on the linear systems theory, (2019).
[22] B. Zhang, J. Ziegert, F. Farahi, A. Davies, In situ surface topography of laser powder bed fusion using fringe projection, Additive Manufacturing 12 (2016) 100-107.
[23] Y. Liu, L. Blunt, Z. Zhang, H.A. Rahman, F. Gao, X. Jiang, In-situ areal inspection of powder bed for electron beam fusion system based on fringe projection profilometry, Additive Manufacturing 31 (2020) 100940.
[24] J.C. Heigel, B.M. Lane, L.E. Levine, In situ measurements of melt-pool length and cooling rate during 3D builds of the metal AM-bench artifacts, Integrating Materials and Manufacturing Innovation 9(1) (2020) 31-53.
[25] M. Halioua, H.-C. Liu, Optical three-dimensional sensing by phase measuring profilometry, Optics and lasers in engineering 11(3) (1989) 185-215.
[26] M. Takeda, K. Mutoh, Fourier transform profilometry for the automatic measurement of 3-D object shapes, Applied optics 22(24) (1983) 3977-3982.
[27] S. Xing, H. Guo, Correction of projector nonlinearity in multi-frequency phase-shifting fringe projection profilometry, Optics express 26(13) (2018) 16277-16291.
[28] L. Huang, P.S. Chua, A. Asundi, Least-squares calibration method for fringe projection profilometry considering camera lens distortion, Applied optics 49(9) (2010) 1539-1548.
[29] G. Wolberg, Digital image warping, IEEE computer society press Los Alamitos, CA1990.
[30] S. Zhang, S.-T. Yau, Generic nonsinusoidal phase error correction for three-dimensional shape measurement using a digital video projector, Applied optics 46(1) (2007) 36-43.
[31] K. Itoh, Analysis of the phase unwrapping algorithm, Applied optics 21(14) (1982) 2470-2470.
[32] Q. Kemao, W. Gao, H. Wang, Windowed Fourier-filtered and quality-guided phase-unwrapping algorithm, Applied optics 47(29) (2008) 5420-5428.
[33] F.A. Morrison, Obtaining uncertainty measures on slope and intercept of a least squares fit with Excel's LINEST, Houghton, MI: Department of Chemical Engineering, Michigan Technological University. Retrieved August 6 (2014) 2015.
[34] R. Leach, Fundamental principles of engineering nanometrology, Elsevier2014.
[35] J. Liang, J. Zhang, J. Shao, B. Song, B. Yao, R. Liang, Deep Convolutional Neural Network Phase Unwrapping for Fringe Projection 3D Imaging, Sensors 20(13) (2020).
[36] H. Zhao, C. Liu, H. Jiang, X. Li, Multisensor registration using phase matching for large-scale fringe projection profilometry, Measurement 182 (2021) 109675.